

Anomalous Dimensionality-Driven Phase Transition of MoTe₂ in Van der Waals Heterostructure

Huije Ryu, Yangjin Lee, Hyun-Jung Kim, Seoung-Hun Kang, Yoongu Kang, Kangwon Kim, Jungcheol Kim, Blanka E. Janicek, Kenji Watanabe, Takashi Taniguchi, Pinshane Y. Huang, Hyeonsik Cheong, In-Ho Jung, Kwanpyo Kim, Young-Woo Son, and Gwan-Hyoung Lee*

Phase transition in nanomaterials is distinct from that in 3D bulk materials owing to the dominant contribution of surface energy. Among nanomaterials, 2D materials have shown unique phase transition behaviors due to their larger surface-to-volume ratio, high crystallinity, and lack of dangling bonds in atomically thin layers. Here, the anomalous dimensionality-driven phase transition of molybdenum ditelluride (MoTe₂) encapsulated by hexagonal boron nitride (hBN) is reported. After encapsulation annealing, single-crystal 2H-MoTe₂ transformed into polycrystalline T_d-MoTe₂ with tilt-angle grain boundaries of 60°-glide-reflection and 120°-twofold rotation. In contrast to conventional nanomaterials, the hBN-encapsulated MoTe₂ exhibit a deterministic dependence of the phase transition on the number of layers, in which the thinner MoTe₂ has a higher 2H-to-T_d phase transition temperature. In addition, the vertical and lateral phase transitions of the stacked MoTe₂ with different crystalline orientations can be controlled by inserted graphene layers and the thickness of the heterostructure. Finally, it is shown that seamless T_d contacts for 2H-MoTe₂ transistors can be fabricated by using the dimensionality-driven phase transition. The work provides insight into the phase transition of 2D materials and van der Waals heterostructures and illustrates a novel method for the fabrication of multi-phase 2D electronics.

1. Introduction


As a wide range of applications has needed scale down of materials, precise control of phase in nanoscale has been more significant. When the size of materials decreases, the large surface-to-volume ratio dramatically changes the phase transition behaviors, leading to stabilize phases under conditions in which they are normally not stable at bulk.^[1–3] Since the increase of surface-to-volume ratio becomes steeper as the materials size down to a few nm scales, the dimensionality control of nanomaterial is important to modulate the phase of it. However, the atomically precise design of dimensionality in 3D nanocrystal is hindered by the limited size controllability and surface reconstruction.^[4–7]

2D materials including layered structure stacked through the van der Waals interaction, for example, graphene, transition metal dichalcogenides (TMDs) such as MoX₂ and WX₂ (X = S, Se, and

H. Ryu, Y. Kang, I.-H. Jung, G.-H. Lee
Department of Materials Science and Engineering
Seoul National University
Seoul 08826, Korea
E-mail: gwanlee@snu.ac.kr

Y. Lee, K. Kim
Department of Physics
Yonsei University
Seoul 03722, Korea

Y. Lee, K. Kim
Center for Nanomedicine, Institute for Basic Science (IBS)
Seoul 03722, Korea

 The ORCID identification number(s) for the author(s) of this article can be found under <https://doi.org/10.1002/adfm.202107376>.

^[†]Present address: Peter Grünberg Institut (PGI-1) and Institute for Advanced Simulation (IAS-1), Forschungszentrum jülich, 52425 Jülich, Germany

H.-J. Kim,^[†] S.-H. Kang, Y.-W. Son
Korea Institute for Advanced Study
Seoul 02455, Korea

K. Kim, J. Kim, H. Cheong
Department of Physics
Sogang University
Seoul 04107, Korea

B. E. Janicek, P. Y. Huang
Department of Materials Science and Engineering
University of Illinois at Urbana–Champaign
Urbana, IL 61801, USA

K. Watanabe
Research Center for Functional Materials
National Institute for Materials Science
Tsukuba 305-0044, Japan

T. Taniguchi
International Center for Materials Nanoarchitectonics
National Institute for Materials Science
Tsukuba 305-0044, Japan

DOI: 10.1002/adfm.202107376

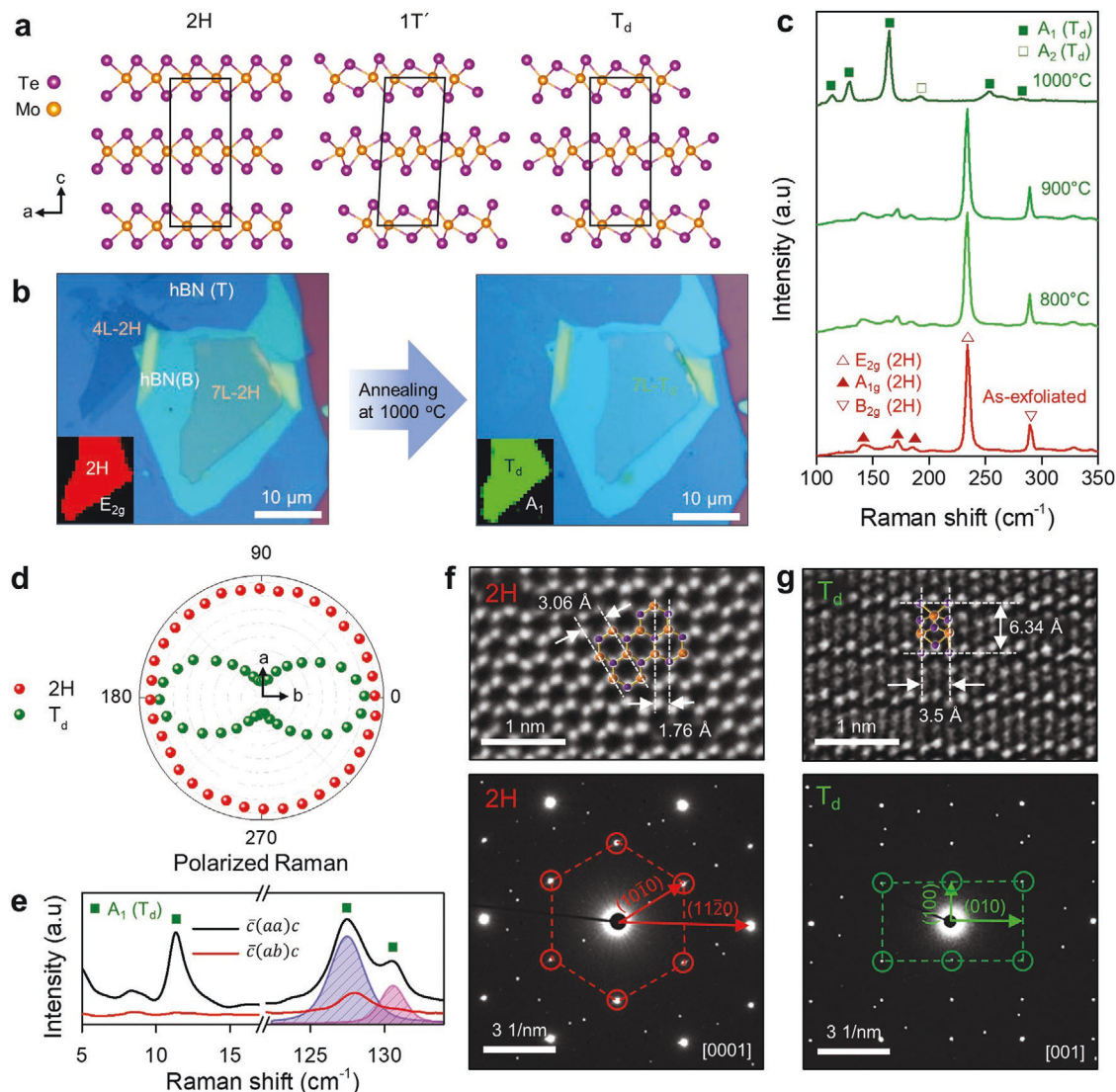


Figure 1. 2H-to- T_d phase transition of MoTe_2 by encapsulation annealing. a) Crystal structures of the 2H, $1T'$, and T_d phase MoTe_2 . b) Optical microscopic images of MoTe_2 before and after encapsulation annealing. The insets are the Raman peak intensity maps for the E_{2g} mode of 2H- MoTe_2 and A_1 mode of T_d - MoTe_2 . c) Raman spectra of the as-exfoliated and annealed 7L- MoTe_2 at different temperatures. d) Polarization-dependent Raman peak intensities of the E_{2g} mode of 2H (235 cm^{-1} , red circles) and A_1 mode of T_d (162 cm^{-1} , green circles). The T_d phase shows the minimum Raman intensity in the two-lobe pattern along the a -axis. e) Low-frequency polarized Raman spectra of annealed MoTe_2 . When the polarization direction of the incident light is parallel to the a -axis of MoTe_2 (indicated by $\bar{c}(aa)c$), the T_d phase exhibits additional Raman peaks of the A_1 mode at 12 cm^{-1} and splitting of the A_1 peak around 127 cm^{-1} for the alignment of aa due to symmetry breaking, which enables us to distinguish the T_d phase from the $1T'$ phase. f, g) HAADF-STEM images and corresponding SAED patterns of graphene encapsulated 2H- MoTe_2 (pre-annealing) and T_d - MoTe_2 (post-annealing), respectively. The molybdenum and tellurium atoms are schematically superimposed with the measured interatomic spacings. The red and green dashed lines indicate the crystal symmetries of the 2H and T_d phases, respectively. The other spots originate from the graphene and multiple scattering at the interfaces.

Te) have been recognized as a promising functional material that can be engineered in atomically-precise limit. Particularly, TMDs have been studied as a promising phase-changeable material. Among them, MoTe_2 has a substantially small phase transition barrier energy than others. MoTe_2 has polymorphs of trigonal prismatic (2H), monoclinic ($1T'$), and orthorhombic (T_d) phases, as depicted in **Figure 1a**. As these polymorphs exhibit distinct electrical properties, the phase transition of MoTe_2 holds great potential for the fabrication of monolithic 2D electronics. So far, various phase transition strategies for

MoTe_2 have been introduced in previous studies such as laser irradiation,^[8] electrostatic doping,^[9] tensile strain,^[10] plasma treatment,^[11] electron beam irradiation,^[12] electric field,^[13,14] and terahertz light field.^[15] Such advances have vast potential for use in new-concept and functional devices such as high-performance field-effect transistors with ultra-low contact resistance,^[8] strain sensor,^[10] and phase-change memory.^[13] However, since these methods accompany deformation of layer structure or incomplete phase transition, there have been a few researches on the dimensionality (thickness and

stacked heterostructure)-dependence of phase transition in 2D materials.

Here, we report the anomalous dimensionality-driven phase transition of MoTe₂ by hBN-encapsulation annealing. Single crystal few-layer 2H-MoTe₂ transformed into polycrystalline T_d-MoTe₂ with well-stitched grain boundaries (GBs). We observed a thickness-dependent transition temperature where the thinner MoTe₂ had a higher transition temperature. We also demonstrate that the vertical and lateral phase transitions of the stacked MoTe₂ flakes can be controlled by inserted graphene layers and the thickness of the heterostructure.

2. Results and Discussion

To investigate the phase transition of MoTe₂, we used encapsulation annealing using hBN. To prevent evaporation of MoTe₂ during annealing, stacks of hBN/MoTe₂/hBN were fabricated by the pick-up technique,^[16] where hBN flakes with a thickness of ≈10 nm were used. The stacks were annealed at 980–1080 °C in a vacuum (see Experimental Section for details on the stacking and annealing processes). Figure 1b shows optical images of hBN-encapsulated MoTe₂ flakes of 4 layers and 7 layers before and after annealing, where the 7L-MoTe₂ was fully encapsulated and 4L-MoTe₂ was partially encapsulated. Although the un-covered 4L-MoTe₂ evaporated entirely, the fully encapsulated 7L-MoTe₂ was preserved after annealing at 1000 °C, which indicates that fully encapsulated MoTe₂ within the hBN is highly stable at high temperatures because of the stability and impermeability of hBN (see the atomic force microscopy images in Figure S1, Supporting Information). For comparison, when the Al₂O₃ film with a thickness of 10 nm was used as the encapsulation layer, the MoTe₂ was degraded during annealing (Figure S2, Supporting Information).

The Raman spectra of the encapsulation-annealed 7L MoTe₂ at different annealing temperatures (T_A) were measured with a 532 nm laser (Figure 1c). When the hBN-encapsulated MoTe₂ was annealed at 800 and 900 °C, the three typical Raman peaks (E_{2g} , A_{1g} , and B_{2g}) of the 2H phase were maintained.^[8,9] However, the annealed MoTe₂ at 1000 °C only exhibited the Raman peaks of the A_1 and A_2 modes of the T_d phase, as indicated by filled and empty square boxes, respectively. To verify the formation of the T_d phase, linear polarized Raman spectroscopy was used in a low-frequency range (Figure 1d,e).^[17,18] The upper and lower insets in Figure 1b show the Raman peak intensity maps for E_{2g} of 2H and A_1 of T_d, respectively. This indicates that 2H-MoTe₂ uniformly transformed into the T_d phase. To confirm the thermal stability of the T_d phase, the transformed T_d-MoTe₂ sample was annealed again at 100–1000 °C. No change in the Raman spectra shows that the T_d phase is highly stable (Figure S3, Supporting Information).

To investigate the crystal structures of MoTe₂ with high-angle annular dark-field scanning transmission electron microscopy (HAADF-STEM), we developed a method to prepare plan-view TEM samples using the graphene etch stop technique (see Figure S4, Supporting Information, for detailed fabrication process).^[19] We fabricated a stack of hBN/Gr/MoTe₂/Gr/hBN by encapsulating MoTe₂ with monolayer graphene and hBN. After annealing, the thick hBN layers were removed by XeF₂

exposure, leaving graphene-encapsulated MoTe₂. In the graphene-encapsulated samples, we can clearly observe the atomic resolution structure of MoTe₂ because of the low contrast of the carbon atoms.^[20] Figure 1f,g shows the HAADF-STEM images and corresponding selected area electron diffraction (SAED) patterns of 2H- and T_d-MoTe₂. As the 1T' and T_d phases have different stacking configurations, as shown by the atomic models in Figure 1a, each phase can be distinguished from out-of-plane HAADF-STEM images.^[21] The well-resolved atom position in Figure 1g clearly shows that the annealed MoTe₂ is a highly crystalline T_d phase with no lattice distortion or massive atomic loss. The d-spacings of the T_d phase calculated from the SAED pattern are well-matched with those in previous studies.^[22,23]

Figure 2a shows the bright-field (BF) and HAADF cross-section STEM images of the 8L-MoTe₂ annealed at 1000 °C. The interfaces between hBN and MoTe₂ are atomically sharp and clean even after annealing. The magnified HAADF-STEM image in Figure 2b shows that the T_d phase formed without any damage or interlayer diffusion. The false-color dark-field transmission electron microscopy (DF-TEM) image in Figure 2c (obtained from the electron diffraction pattern in Figure 2d) shows that the transformed T_d-MoTe₂ consists of multiple micrometer-sized grains well-stitched along the straight GBs, which is in agreement with the theoretical prediction.^[24,25] T_d-MoTe₂ forms a unique polycrystalline structure of polygonal grains and sharp GBs to reduce the interface energy of the GBs with misfit strain by the Wulff construction. The different colors of grains in the DF-TEM image were determined from three selected spots of the electron diffraction pattern. The three selected patterns have only an angle difference of 60°. The crystal structure of 2H-MoTe₂ is threefold symmetric; as a result, the glide of atomic planes along the three different armchair directions of 2H-MoTe₂ produces polycrystalline T_d-MoTe₂, which has only a 60° difference in all grains.^[9,12]

We performed first-principles calculations to find out the optimal atomic configurations of GBs in polycrystalline T_d-MoTe₂. As consistent with an earlier study on GBs in a single layer MoTe₂,^[24] our multilayers also show that the [010] directions of contiguous grains at the GBs have angles of 60° or 120° as shown in Figure 2e,f. Our total energy calculations of several inequivalent symmetric tilt GBs in bulks also prefer 120°-two-fold-rotation GB and 60°-glide-reflection GB over the other configurations. We also found that the GBs in the adjacent layers slightly avoid each other by shifting themselves in a direction parallel to the layer to reduce their total energy (see details in Figure S5, Supporting Information).

We also observed that the phase transition temperature (T_{PT}) of hBN-encapsulated MoTe₂ increases with a decreasing number of layers. When the MoTe₂ flake with regions of different thicknesses was annealed at 995 °C, the thicker regions underwent a 2H-to-T_d transition, while the 2L region remained in the 2H phase, as shown in the optical images and corresponding Raman intensity map of Figure 3a,3b. The schematic of Figure 3c shows that the phase of MoTe₂ can be spatially defined by a thickness-dependent phase transition. By encapsulating a number of samples with different thicknesses, constructed a phase diagram of MoTe₂, as shown in Figure 3d. As the number of layers decreases, T_{PT} increases in steps. It should be noted that the transition temperature gaps increase

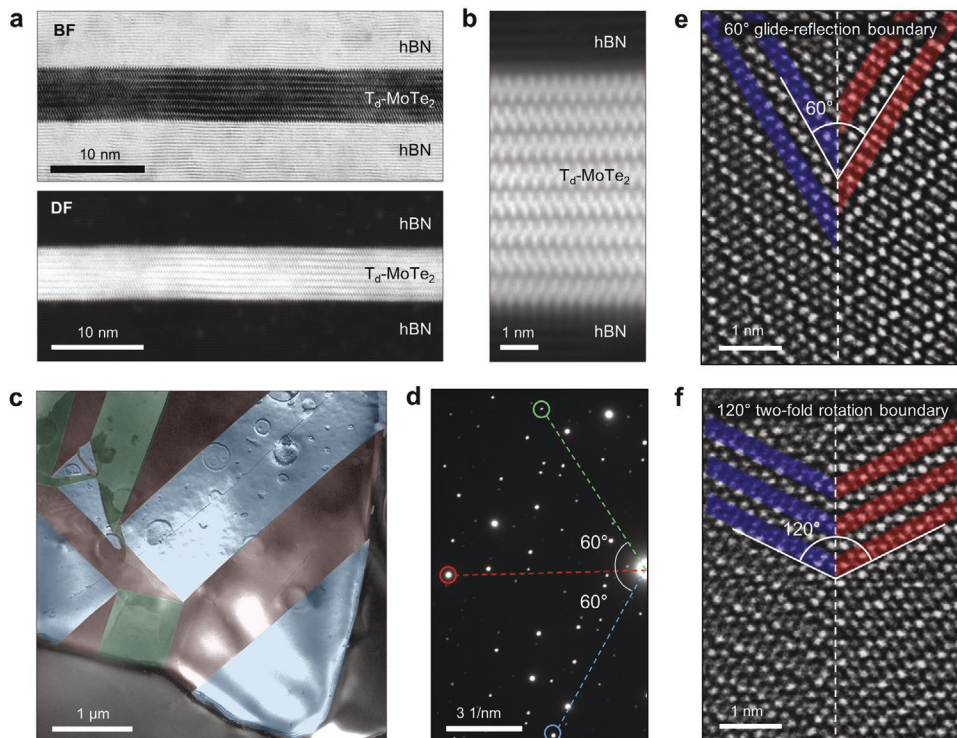


Figure 2. Atomic structure and polycrystalline structure of transformed T_d - MoTe_2 . a) Low-magnification cross-section BF- and HAADF-STEM images of $\text{hBN}/T_d\text{-MoTe}_2/\text{hBN}$. b) Magnified image of cross-section HAADF STEM image. The interface between MoTe_2 and hBN is ultraclean, and there is no atomic diffusion observed after high-temperature annealing. c) False-color DF-TEM images of T_d MoTe_2 . d) SAED pattern of polycrystalline T_d - MoTe_2 in Figure 2c. Polycrystalline T_d - MoTe_2 has only a 60° difference in all of the grains. As single-crystalline 2H-MoTe_2 has threefold armchair directions, armchair direction aligned atomic plane sliding results in a polycrystalline T_d - MoTe_2 that has only a 60° difference in all of the grains. e) HAADF-STEM image of the 60° glide-reflection GB of polycrystalline T_d - MoTe_2 . f) HAADF-STEM image of 120° twofold rotation GB.

from 1°C for 6–7L to 77°C for 1–2L as shown in the inset of Figure 3d. The large temperature difference in a few atom-thick ranges enables precise control of the phase transition in ultrathin layered materials. As described in Figure 3e,f, the conventional nanoparticles with a broad size distribution around b_1 and b_2 have a large overlap in the phase transition temperature ranges around $T_{\text{PT},b1}$ and $T_{\text{PT},b2}$ so that it is difficult to selectively induce phase transition for the desired nanoparticles with specific size. However, the MoTe_2 sheets with discrete thickness differences (a_1 and a_2) of atomically defined distribution have distinct phase transition temperatures of $T_{\text{PT},a1}$ and $T_{\text{PT},a2}$, which enables precise control of phase transition by the thickness of MoTe_2 .

The increase of T_{PT} with decreasing thickness of MoTe_2 is due to the significant contribution of the surface energy in the nucleation and growth of the newly formed phase. To clarify this, we assumed a model which has a thin cylindrical disc-type nucleus. The calculated bulk energy of T_d is smaller than that of 2H over the transition temperature. Therefore, an inverse relation between T_{PT} and thickness indicates that T_d should have a larger surface energy than 2H . As a result, thinner MoTe_2 requires a larger critical radius of the 2D nucleus (r^*) and larger activation Gibbs free energy (ΔG^*) for the growth of T_d . As predicted, we revealed that the surface energy of T_d phase is larger than that of the 2H phase by calculating the surface energies from the transition temperatures of Figure 3d. (see details in Figure S6, Supporting Information). However, the large transition

temperature difference between the monolayer and bilayer, which deviates from the theoretical prediction that accounts only for surface and activation energies (inset of Figure S6d, Supporting Information). Instead, we found that additional factors, such as charge carrier density and pressure, must be taken into account to explain the anomalously high phase transition temperature for monolayer MoTe_2 . First, during the thermal expansion of encapsulated MoTe_2 at high temperatures, MoTe_2 is compressed along the c -axis because the hBN encapsulation limits the volume expansion of MoTe_2 . Second, the charge carriers of both electrons and holes are thermally excited in MoTe_2 . Our first-principles calculations reveal that the applied pressure reduces the energy of T_d , and the increased charge carrier density lowers the barrier energy for the phase transition (Figure S7, Supporting Information). It is estimated that the monolayer has a smaller pressure than the thicker. Moreover, the monolayer has a smaller density of thermally excited electrons and holes at the fixed temperature than the thicker because of the larger bandgap.^[26] Therefore, the monolayer needs a much higher temperature for the 2H -to- T_d transition, probably due to the combinational effect of the smaller charge carrier density and reduced pressure in the vdW heterostructures.

Notably, we observe an increase in phase transition temperature for thinner layers, a result that stands in stark opposition to the trends in phase stability of conventional nanocrystals, which exhibit a decrease in T_{PT} with decreasing size (Figure S8, Supporting Information).^[27–34] These results indicate

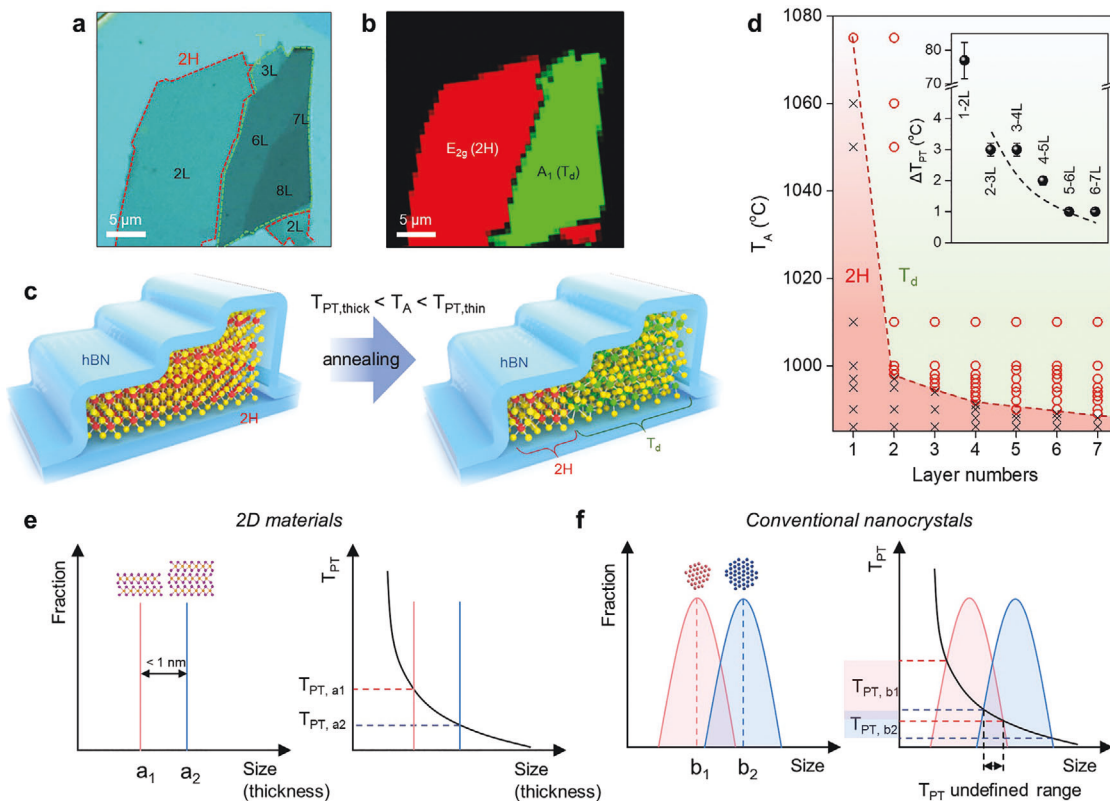


Figure 3. Thickness-dependent phase transition of MoTe₂. a,b) Optical microscopic image and corresponding Raman peak intensity map of hBN-encapsulated MoTe₂ with various thicknesses after hBN encapsulation annealing at 995 °C. The Raman peak intensity map was obtained from the E_{2g} mode of 2H and A₁ mode of T_d. c) Schematic illustration of the thickness-dependent phase transition of hBN-encapsulated MoTe₂. If the T_A is higher than the T_{PT} of thin MoTe₂ (T_{PT,thin}) and lower than that of the thick one (T_{PT,thick}), the phase transition occurs only in the thick region. d) Phase diagram of the 2H and T_d phases in the hBN-encapsulated MoTe₂. The red circles indicate that the MoTe₂ exhibited phase transition at the T_A. The T_{PT} substantially increased from 989 °C for 7L to 1075 °C for 1L as the number of layers decreased. Inset: T_{PT} increasing steps as a function of layer difference. The black dashed curve is a guide to the eye. e,f) Conceptual diagram about size-dependent phase transition temperature (T_{PT}) distributions in 2D materials and conventional nanocrystals.

differences in the mechanisms of phase transition between the 2D materials and conventional nanocrystals. Nucleation of the newly formed phase in conventional nanocrystals generally occurs on a disordered surface, which would promote nucleation in smaller nanocrystals regardless of the surface energy difference.^[27–29,35]

To investigate the effect of dimensionality, such as the thickness and stacking order of the vdW heterostructure, on the phase transition of MoTe₂, we fabricated a randomly stacked heterostructure of two MoTe₂ flakes with different thicknesses. Monolayer graphene was partially inserted to weaken the coupling between stacked MoTe₂ layers, as depicted in **Figure 4a**. **Figure 4b** shows the optical images and Raman intensity maps of the annealed graphene-inserted heterostructure of 2L- and 8L-MoTe₂ at 995 °C, which is higher than the T_{PT} of 8L (T_{PT,8L}) and lower than that of 2L (T_{PT,2L}). Detailed Raman spectra in each area are depicted in **Figure S9**, Supporting Information. The heterostructure consists of four areas: hBN/8L-MoTe₂/Gr/2L-MoTe₂/hBN, hBN/8L-MoTe₂/2L-MoTe₂/hBN, hBN/8L-MoTe₂/hBN, and hBN/2L-MoTe₂/hBN (denoted as B8MG2MB, B8M2MB, B8MB, and B2MB, respectively). Raman intensity maps for the E_{2g} mode of 2H-MoTe₂ and the A₁ mode of T_d-MoTe₂ reveal that the stacked and 8L areas transformed into

the T_d phase, except for the 2L region. Note that the misaligned stacked region of 2L and 8L totally transformed into T_d even at the T_A lower than T_{PT,2L}. Furthermore, the B8MG2MB region, where the graphene is inserted between 2L and 8L, showed both Raman peaks of 2H and T_d, indicating the coexistence of 2H and T_d.

To verify the effect of the inserted graphene on the phase transition, we measured the SAED patterns of the B8M2MB and B8MG2MB regions. In the B8M2MB region, only signals of a single T_d phase were observed without any remaining 2H phase, as indicated by the green rectangle in **Figure 4c**. Several diffraction spots are originated from hBN and multiple scattering at the heterointerface.^[36] This result reveals that, as depicted in **Figure 4d**, the 2L region changed to the T_d phase with the same crystalline alignment to the 8L region, despite a twist angle of 8° in the as-stacked sample. The stacked crystals appeared to rotate reduce the interfacial energy induced by misalignment with the help of pressure and thermal energy during the annealing process.^[37,38] Meanwhile, the graphene-inserted heterostructure of B8MG2MB exhibited SAED patterns of both 2H and T_d phases with misalignment, as shown in **Figure 4e**. Only 8L-MoTe₂ transformed into T_d, and there was no phase transition or crystalline rotation of the 2L-MoTe₂ owing to

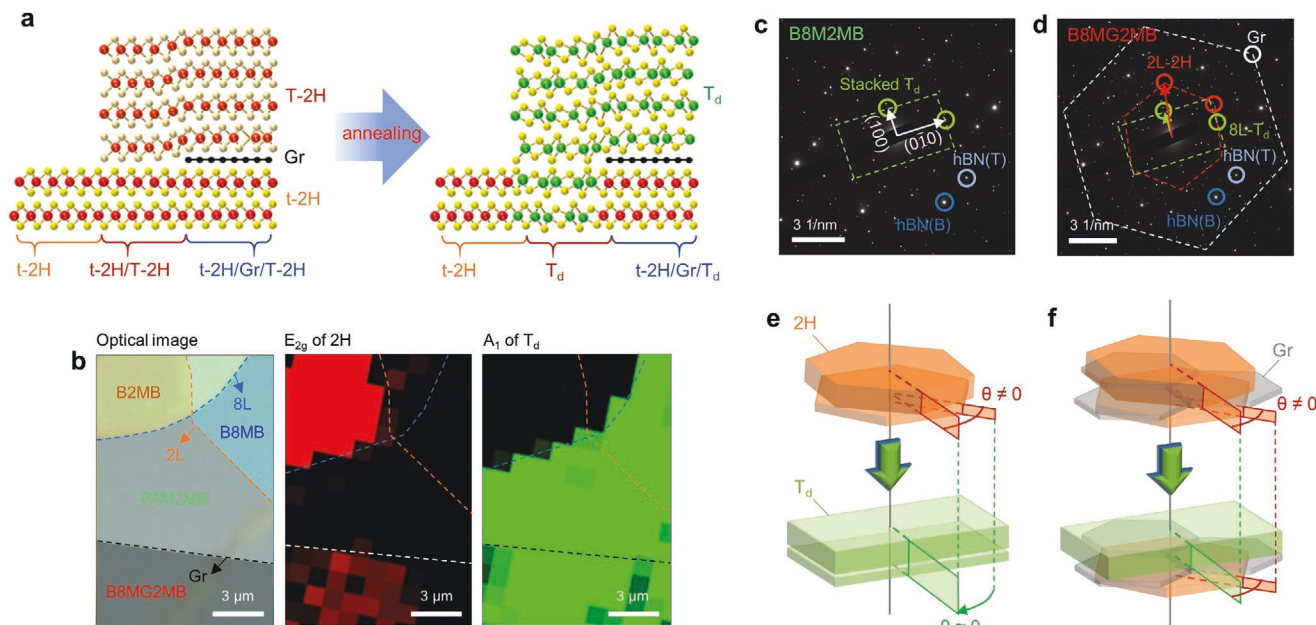


Figure 4. Phase transition of the stacked MoTe₂ layers with an inserted monolayer graphene. a) Phase transition process of the randomly stacked MoTe₂ flakes with an inserted monolayer graphene. The thin and thick 2H-MoTe₂ with different phase transition temperatures are denoted as t-2H and T-2H, respectively. When the stack was annealed at $T_{PT,thick} < T_A < T_{PT,thin}$, the stacked and thick regions (t-2H/T-2H and T-2H) were changed to the T_d phase, except for the thin region and graphene-inserted region. b) Optical image and Raman intensity mapping images of annealed monolayer graphene inserted thin MoTe₂/thick MoTe₂ heterostructure. B8MG2MB, B8M2MB, B8MB, and B2MB indicate the areas of hBN/MoTe₂(8L)/Gr/MoTe₂(2L)/hBN, hBN/MoTe₂(8L)/MoTe₂(2L)/hBN, hBN/MoTe₂(8L)/hBN, and hBN/MoTe₂(2L)/hBN. Under annealing at the temperature where B2MB does not change its phase, phase transition occurred at B8MB, B8M2MB, and B8MG2MB. c, d) Selective area electron diffraction patterns in B8M2MB, and B8MG2MB. After annealing, the misaligned stack of 2L and 8L of 2H-MoTe₂ with a twist angle transforms into aligned T_d-MoTe₂ with zero twist angle. e, f) Schematic illustrations of the crystal orientation rotation of B8M2MB and B8MG2MB. Inserted graphene hindered coupled phase transition phenomena, which could result from increased interface energies for MoTe₂(2L)/Gr and MoTe₂(8L)/Gr.

the weakened coupling between 2L- and 8L-MoTe₂ due to the inserted graphene, as shown in Figure 4f. Therefore, this result indicates that the phase transition of MoTe₂ in the vdW heterostructure can be controlled by the dimensionality of thickness and stacking order, which enables phase patterning of MoTe₂ along the lateral and vertical directions.

We measured the electrical properties of the transformed T_d phase. T_d-MoTe₂ of 7L is completely metallic with a low resistivity of $6.7 \times 10^{-3} \Omega \text{ cm}$, which is similar to a previously measured value (Figure 5a–d).^[39] To fabricate 2H-MoTe₂ transistors with T_d contacts, we utilized the dimensionality-driven phase patterning technique. By annealing the as-exfoliated 2H-MoTe₂ consisting of 2L and 8L regions, we fabricated 8L-T_d contacts for the 2L-2H channel as shown in Figure 5e, f. (See Figure S10, Supporting Information, for device fabrication process) The device showed typical ambipolar transport behavior with linear I_{DS} - V_{DS} curves, indicating that ohmic contacts formed at the lateral junction of 2H and T_d. The field-effect mobility (μ_{eff}) of hole is $7.86 \text{ cm}^2 \text{ Vs}^{-1}$. The contact resistance of 2H-T_d junction calculated by the Y-function method^[40] is $372 \Omega \mu\text{m}$ (see Supplementary Information for details of the calculation). This value is comparable to the low contact resistances of the metallic phase contacts of 1T through lithiation^[41] and 1T' through electrical breakdown and CVD synthesis.^[42,43] We also fabricated the T_d contacts by using vertical phase patterning. As shown in Figure S10, Supporting Information, we transferred two 5L MoTe₂ flakes on both ends of 2L MoTe₂, followed by encapsulation

annealing. At an intermediate transition temperature of 990°C (lower than $T_{PT,2L}$, but higher than $T_{PT,7L}$), the stacked regions were changed to T_d phase, maintaining the 2L channel unchanged (see Figure S11, Supporting Information). The heterophase MoTe₂ devices fabricated by vertical phase patterning also showed similar device performances.

3. Conclusion

In conclusion, we have demonstrated an anomalous dimensionality-driven phase transition of MoTe₂ by using encapsulated annealing within hBN. We transformed the single-crystalline 2H-MoTe₂ into high-quality polycrystalline T_d-MoTe₂, which only has a 60° difference in all the grains. Phase transition of MoTe₂ has thickness-dependence; T_{PT} increases with decreasing number of layers due to the highly ordered surface structure of MoTe₂ with no dangling bonds and higher surface energy of T_d-MoTe₂ than 2H-MoTe₂. The thickness-dependent phase transition occurs even in a stack of two MoTe₂ flakes with different crystallographic orientations. The coupled phase transition can be controlled by inserting monolayer graphene between stacked MoTe₂ flakes. The dimensionality-driven phase transition of MoTe₂ in van der Waals heterostructure opens new possibilities for developing 3D phase patterning and monolithic 2D electronic devices consisting of different phases of the same 2D materials.

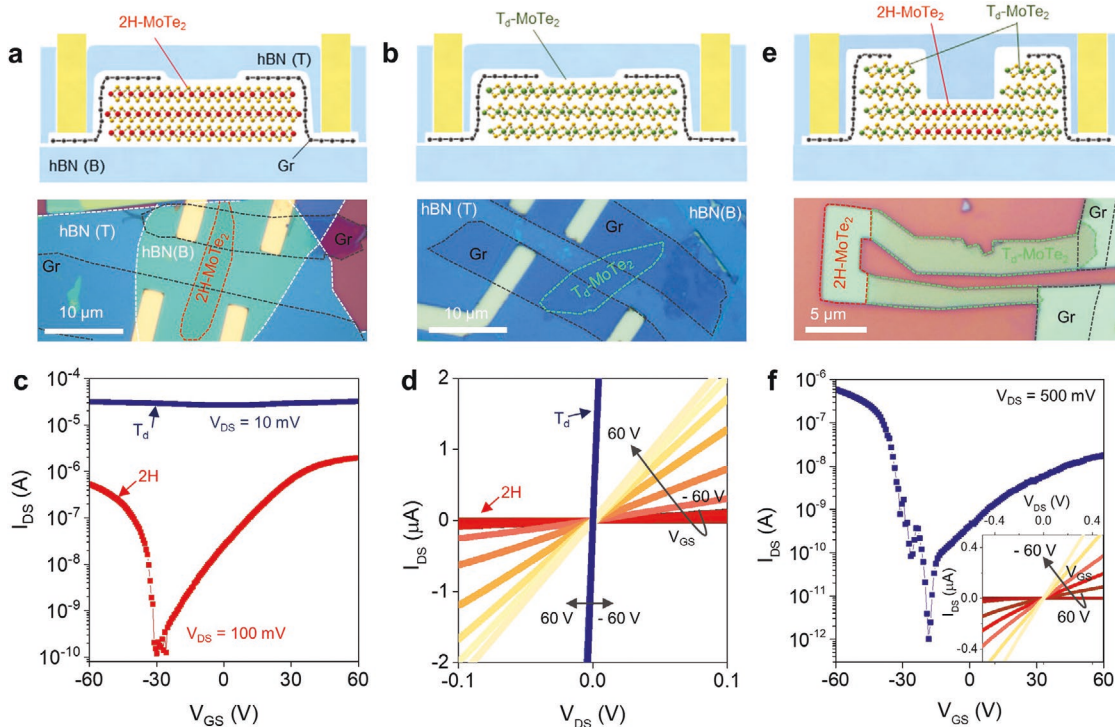


Figure 5. Phase-engineered 2H-MoTe₂/T_d-MoTe₂ heterophase devices. a,b) Schematic illustrations and optical microscope images of hBN-encapsulated 2H-MoTe₂ and T_d-MoTe₂ devices with graphene contacts. c) I_{DS} - V_{GS} characteristics for 2H- and T_d-MoTe₂ channel devices. The 2H-MoTe₂ device showed an ambipolar semiconducting characteristics, meanwhile T_d-MoTe₂ showed high I_{DS} without gate dependence, which indicates that T_d-MoTe₂ is metallic. d) I_{DS} - V_{DS} characteristics for 2H- and T_d-MoTe₂ channel devices as a function of back-gate voltage V_{GS} ranging from -60 to 60 V. e) Schematic representation and optical microscope image of a device with the T_d-2H monolithic heterophase junction in MoTe₂. f) I_{DS} - V_{GS} characteristics for a monolithic heterophase junction device as a function of back-gate voltage V_{GS} ranging from -60 to 60 V. The device has semiconducting characteristics with a current I_{on}/I_{off} of 10^6 . The inset shows a linear behavior in the I_{DS} - V_{DS} curves, indicating that typical ohmic contact formed at the junction of 2H and T_d.

4. Experimental Section

Stacking Process and Encapsulation Annealing: All 2D flakes used for fabrication were mechanically exfoliated onto SiO₂/Si substrates. The thickness of each material was separately confirmed using a combination of AFM and optical contrast. To encapsulate MoTe₂ between hBN, the pick-up transfer technique was used with a polypropylene carbonate (bisphenol A carbonate, Sigma Aldrich) (PC)-coated poly (dimethyl siloxane) (PDMS) lens mounted on a slide glass to pick-up and release.^[16] The PDMS/PC/slide glass was held in a 3-axis micromanipulator to control the position of the contact area. By only controlling the temperature of the stage (80–130 °C), the top hBN was picked up completely by the PC without cracking or folding. After detaching hBN from the substrates, MoTe₂ and the bottom hBN were picked-up by van der Waals forces from the top hBN to form hBN/MoTe₂/hBN ultrathin 2D heterostructures. Note that MoTe₂ must be fully encapsulated by hBN without bubbles. Otherwise, MoTe₂ was degraded during the annealing process. After stacking, the heterostructure was transferred onto a clean SiO₂/Si substrate by releasing the PC film from the PDMS lens at a temperature above 180 °C. Finally, in order to remove the PC film, the samples in chloroform were placed for 30 min. For the phase transition of MoTe₂, the sandwiched MoTe₂ was annealed in a vacuum of 10^{-4} Torr. The furnace temperature was ramped up to the target annealing temperature for 3 h and maintained for 3 h. Then, the furnace was naturally cooled to room temperature.

Raman Spectroscopy: The Raman spectra in Figure 1c were acquired using Raman spectroscopy (Renishaw) with a 532 nm laser. To minimize the damage of the sample by irradiation of the laser, a power of <5 mW was used with an acquisition time of 60 s. Since the laser spot size was about 1 μm, mapping area was scanned with 1 μm point-to-point distance. All measurements were conducted at room temperature after

cooling down the annealed samples. The linearly polarized Raman measurements (Figure S3, Supporting Information) were carried out in the backscattering geometry using 514.5 nm laser excitation. The input laser beam was focused onto the samples by a 40× microscope objective lens (0.6 NA), and the scattered light was collected and collimated by the same objective lens. To access the low-frequency range below 50 cm⁻¹, volume holographic filters (Optigrade) were used to clean the laser lines and reject the Rayleigh-scattered light. A laser with a power below 200 μW was used to avoid local heating. The Raman scattering signals were dispersed by a Jobin-Yvon iHR550 spectrometer with a 2400 grooves mm⁻¹ grating (400 nm blaze) and detected by a liquid-nitrogen-cooled back-illuminated charge-couple-device (CCD) detector. An achromatic half-wave plate was used to rotate the polarization of the linearly polarized laser beam to the desired direction. The analyzer angle was set such that photons with polarization parallel or perpendicular to the incident polarization passed through. Another achromatic half-wave plate was placed in front of the spectrometer to keep the polarization direction of the signal entering the spectrometer constant with respect to the groove direction of the grating. The crystal orientation of T_d-MoTe₂ was identified using an anisotropic polarized Raman response.^[44,45]

Transmission Electron Microscopy: TEM and HAADF-STEM images were acquired to confirm the crystal structure and crystallographic orientations of T_d-MoTe₂. TEM samples were prepared using the poly (methyl methacrylate) (PMMA)-based transfer method. Samples on PMMA film were transferred to holey Si₃N₄ TEM grids (TED PELLA, 21581-10) and Si₃N₄ nanofilm TEM grids (TEM Windows, SN100-A10Q33B). Then, the PMMA film was removed by placing the samples in acetone for 12 h. Bright-/dark-field TEM images and SAED patterns were acquired using the JEOL-2100Plus at an operating voltage of 200 kV. DF-TEM images were taken using an objective aperture with a 1.22 nm⁻¹ diameter for an acquisition time of 5 s. A double-Cs-aberration-corrected

JEOL ARM-200F was used for HAADF-STEM images at an operating voltage of 80 kV with a 23 mrad convergence angle and collection semi-angles from 68 to 280 mrad. Cross-section TEM samples were prepared by evaporating a 10 nm protective layer of amorphous carbon on top of the heterostructure, followed by using standard focused ion beam lift-out procedures in an FEI Helios 600i Dual Beam FIB-SEM. Final milling was performed at 2 kV with a cryo-finger inserted to minimize damage and redeposition. Samples were imaged in a Thermo Fisher Scientific Themis-Z aberration-corrected STEM operated at 80 kV with a 25 mrad convergence angle.

First-Principles Calculations: Massive first-principles computations were performed on the stability of GBs across the layers in T_d -MoTe₂. First, the GB structures were fully relaxed in a single layer T_d -MoTe₂ and then stacked the relaxed layers. To deal with a large number of atoms with GBs (≈ 2000), the single zeta polarized pseudo-atomic orbitals were employed as the wave function basis set, as implemented in the SIESTA code.^[25,46] The generalized gradient approximation was used for the exchange and correlation energy functional.^[47] A simple van der Waals correction scheme (PBE+D2) was also used, which reproduces the experimental value of the interlayer distance in bulk MoTe₂ without GBs.^[48,49] The norm-conserving Troullier–Martins pseudopotential with a scalar-relativistic effect in the Kleinman–Bylander factorized form was used for ionic interaction.^[50,51] The energy cutoff for the charge density integration was 450 Ry, achieving total energy convergence within 1 meV atom⁻¹. A rectangular supercell was used with two GBs for the periodic boundary condition. The k-grids of $1 \times 5 \times 4$ and $1 \times 3 \times 4$ were used for sampling the Brillouin zone (BZ) for the bulk T_d -MoTe₂ structures with the 120° and 60° GBs, respectively.

To investigate the phase transition of bulk MoTe₂ between 2H and T_d , ab initio calculations were performed as implemented in the VASP code.^[52,53] Projector augmented wave potentials^[52,53] were employed to describe the valence electrons, and the electronic wave functions were expanded by a plane wave basis set with a cutoff energy of 450 eV, and the atomic relaxation was continued until the Hellmann–Feynman force acting on every atom was lower than 0.005 eV Å⁻¹. For the exchange-correlation functional, the rev-vdW-DF2 method was used,^[54] which was known to be suitable for computing atomic structures of layered TMDs.^[49] The BZ was sampled using a $16 \times 32 \times 8$ k-grid for the primitive unit cells. All parameters have been thoroughly tested to describe the structures and energies of the 1T' MoTe₂ single layer. To simulate the pressure effect with the hBN encapsulation, the lattice parameter was adjusted along the c-direction for a given pressure accordingly. To simulate the effect of charge carrier generation at a finite temperature, the Fermi–Dirac smearing method was used as was used in the other study.^[15]

Device Fabrication and Electrical Measurement: E-beam lithography was performed to develop patterns of metal pads and create a via-contact for graphene electrodes encapsulated by hBN. The van der Waals heterostructure was etched by exposing the pre-patterned structure to XeF₂.^[19] The top hBN was etched away, and the embedded graphene electrodes stopped the etching process. Metals of Cr/Pd/Au (1nm/30nm/40nm) were then deposited on the exposed graphene electrodes using an e-beam evaporator. Finally, a lift-off process was performed on the samples by soaking them in acetone. The electrical measurements of the devices were conducted using a parameter analyzer (Keithley 2400) at room temperature under ambient conditions.

Supporting Information

Supporting Information is available from the Wiley Online Library or from the author.

Acknowledgements

This work was supported by the National Research Foundation (NRF) of Korea (2018M3D1A1058793, 2017R1A5A1014862 (SRC Program: vdWMRC

Center)) and the Creative-Pioneering Researchers Program through Seoul National University (SNU). Y.-W.S. was supported by the KIAS individual Grant. No. CG031509. Computations were supported by the CAC of KIAS. Y.L. and K.K. acknowledge support from the Institute for Basic Science (IBS-R026-D1). Y.L. received support from the Basic Science Research Program at the National Research Foundation of Korea which was funded by the Ministry of Education (NRF-2020R1A6A3A13060549) and Ministry of Science and ICT (NRF-2021R1C1C2006785). B.E.J. and P.Y.H. acknowledge funding support by NSF-MRSEC award number DMR-1720633 and the use of the University of Illinois Shared Facilities. H.-J.K. acknowledges support from the POSCO Science Fellowship of POSCO TJ Park Foundation and from the Alexander von Humboldt Foundation.

Conflict of Interest

The authors declare no conflict of interest.

Data Availability Statement

Research data are not shared.

Keywords

2D materials, dimensionality, MoTe₂, phase transition, van der Waals heterostructures

Received: July 29, 2021

Revised: August 26, 2021

Published online:

- [1] S. H. Tolbert, A. P. Alivisatos, *Science* **1994**, 265, 373.
- [2] A. N. Goldstein, C. M. Echer, A. P. Alivisatos, *Science* **1992**, 256, 1425.
- [3] J. M. McHale, *Science* **1997**, 277, 788.
- [4] J. Park, K. An, Y. Hwang, J. G. Park, H. J. Noh, J. Y. Kim, J. H. Park, N. M. Hwang, T. Hyeon, *Nat. Mater.* **2004**, 3, 891.
- [5] J. Piella, N. G. Bastús, V. Puentes, *Chem. Mater.* **2016**, 28, 1066.
- [6] K. D. Gilroy, A. O. Elnabawy, T. H. Yang, L. T. Roling, J. Howe, M. Mavrikakis, Y. Xia, *Nano Lett.* **2017**, 17, 3655.
- [7] X. Zhu, Z. Zhang, J. Zhu, S. Zhou, Z. Liu, *J. Cryst. Growth* **2009**, 311, 2437.
- [8] S. Cho, S. Kim, J. H. Kim, J. Zhao, J. Seok, D. H. Keum, J. Baik, D. H. Choe, K. J. Chang, K. Suenaga, S. W. Kim, Y. H. Lee, H. Yang, *Science* **2015**, 349, 625.
- [9] Y. Wang, J. Xiao, H. Zhu, Y. Li, Y. Alsaïd, K. Y. Fong, Y. Zhou, S. Wang, W. Shi, Y. Wang, A. Zettl, E. J. Reed, X. Zhang, *Nature* **2017**, 550, 487.
- [10] S. Song, D. H. Keum, S. Cho, D. Perello, Y. Kim, Y. H. Lee, *Nano Lett.* **2016**, 16, 188.
- [11] H. Nan, J. Jiang, S. Xiao, Z. Chen, Z. Luo, L. Zhang, X. Zhang, H. Qi, X. Gu, X. Wang, Z. Ni, *Nanotechnology* **2019**, 30, 034004.
- [12] Y. C. Lin, D. O. Dumcenco, Y. S. Huang, K. Suenaga, *Nat. Nanotechnol.* **2014**, 9, 391.
- [13] F. Zhang, H. Zhang, S. Krylyuk, C. A. Milligan, Y. Zhu, D. Y. Zemlyanov, L. A. Bendersky, B. P. Burton, A. V. Davydov, J. Appenzeller, *Nat. Mater.* **2019**, 18, 55.
- [14] C. Kim, S. Issarapanacheewin, I. Moon, K. Y. Lee, C. Ra, S. Lee, Z. Yang, W. J. Yoo, *Adv. Electron. Mater.* **2020**, 6, 1900964.
- [15] J. Shi, Y. Q. Bie, W. Chen, S. Fang, J. Han, Z. Cao, T. Taniguchi, K. Watanabe, V. Bulović, E. Kaxiras, P. Jarillo-Herrero, K. A. Nelson, *Terahertz Driven Reversible Topological Phase Transition of Monolayer*

- Transition Metal Dichalcogenides* **2019**, <https://doi.org/10.1002/adv.202003832>.
- [16] L. Wang, I. Meric, P. Y. Huang, Q. Gao, Y. Gao, H. Tran, T. Taniguchi, K. Watanabe, L. M. Campos, D. A. Muller, J. Guo, P. Kim, J. Hone, K. L. Shepard, C. R. Dean, *Science* **2013**, *342*, 614.
- [17] K. Zhang, C. Bao, Q. Gu, X. Ren, H. Zhang, K. Deng, Y. Wu, Y. Li, J. Feng, S. Zhou, *Nat. Commun.* **2016**, *7*, 13552.
- [18] Y. Cheon, S. Y. Lim, K. Kim, H. Cheong, *ACS Nano* **2021**, *15*, 2962.
- [19] J. Son, J. Kwon, S. Kim, Y. Lv, J. Yu, J. Y. Lee, H. Ryu, K. Watanabe, T. Taniguchi, R. Garrido-Menacho, N. Mason, E. Ertekin, P. Y. Huang, G. H. Lee, A. M. van der Zande, *Nat. Commun.* **2018**, *9*, 3988.
- [20] K. Elibol, T. Susi, G. Argentero, M. R. A. Monazam, T. J. Pennycook, J. C. Meyer, J. Kotakoski, *Chem. Mater.* **2018**, *30*, 1230.
- [21] J. Cui, P. Li, J. Zhou, W. Y. He, X. Huang, J. Yi, J. Fan, Z. Ji, X. Jing, F. Qu, Z. G. Cheng, C. Yang, L. Lu, K. Suenaga, J. Liu, K. T. Law, J. Lin, Z. Liu, G. Liu, *Nat. Commun.* **2019**, *10*, 2044.
- [22] J. C. Park, S. J. Yun, H. Kim, J. H. Park, S. H. Chae, S. J. An, J. G. Kim, S. M. Kim, K. K. Kim, Y. H. Lee, *ACS Nano* **2015**, *9*, 6548.
- [23] R. Sankar, G. N. Rao, I. P. Muthuselvam, C. Butler, N. Kumar, G. S. Murugan, C. Shekhar, T. R. Chang, C. Y. Wen, C. W. Chen, W. L. Lee, M. T. Lin, H. T. Jeng, C. Felser, F. C. Chou, *Chem. Mater.* **2017**, *29*, 699.
- [24] J. Berry, S. Zhou, J. Han, D. J. Srolovitz, M. P. Haataja, *Phys. Rev. Mater.* **2018**, *2*, 114002.
- [25] H. W. Kim, S. H. Kang, H. J. Kim, K. Chae, S. Cho, W. Ko, S. Jeon, S. H. Kang, H. Yang, S. W. Kim, S. Park, S. Hwang, Y. K. Kwon, Y. W. Son, *Nano Lett.* **2020**, *20*, 5837.
- [26] K. F. Mak, C. Lee, J. Hone, J. Shan, T. F. Heinz, *Phys. Rev. Lett.* **2010**, *105*, 136805.
- [27] W. Zhang, Y. Xue, Q. Fu, Z. Cui, S. Wang, *Powder Technol.* **2017**, *308*, 258.
- [28] M. Wang, Y. Xue, Z. Cui, R. Zhang, *J. Phys. Chem. C* **2018**, *122*, 8621.
- [29] Z. Cui, H. Duan, Q. Fu, Y. Xue, S. Wang, *J. Phys. Chem. C* **2017**, *121*, 24831.
- [30] D. Li, G. Wang, H. C. Cheng, C. Y. Chen, H. Wu, Y. Liu, Y. Huang, X. Duan, *Nat. Commun.* **2016**, *7*, 11330.
- [31] L. Liu, R. Zhao, C. Xiao, F. Zhang, F. Pevere, K. Shi, H. Huang, H. Zhong, I. Sychugov, *J. Phys. Chem. Lett.* **2019**, *10*, 5451.
- [32] J. B. Rivest, L. K. Fong, P. K. Jain, M. F. Toney, A. P. Alivisatos, *J. Phys. Chem. Lett.* **2011**, *2*, 2402.
- [33] N. Satoh, T. Nakashima, K. Yamamoto, *Sci. Rep.* **2013**, *3*, 1959.
- [34] T. Hu, J. S. Wittenberg, A. M. Lindenberg, *Nanotechnology* **2014**, *25*, 415705.
- [35] A. Kovács, K. Sato, V. K. Lazarov, P. L. Galindo, T. J. Konno, Y. Hirotsu, *Phys. Rev. Lett.* **2009**, *103*, 115703.
- [36] A. W. Tsen, R. Hovden, D. Wang, Y. D. Kim, J. Okamoto, K. A. Spoth, Y. Liu, W. Lu, Y. Sun, J. C. Hone, L. F. Kourkoutis, P. Kim, A. N. Pasupathy, *PNAS* **2015**, *112*, 15054.
- [37] X. Zhao, Y. Ji, J. Chen, W. Fu, J. Dan, Y. Liu, S. J. Pennycook, W. Zhou, K. P. Loh, *Adv. Mater.* **2019**, *31*, 1900237.
- [38] S. Zhu, P. Pochet, H. T. Johnson, *ACS Nano* **2019**, *13*, 6925.
- [39] Y. Qi, P. G. Naumov, M. N. Ali, C. R. Rajamathi, W. Schnelle, O. Barkalov, M. Hanfland, S. C. Wu, C. Shekhar, Y. Sun, V. Süß, M. Schmidt, U. Schwarz, E. Pippel, P. Werner, R. Hillebrand, T. Förster, E. Kampert, S. Parkin, R. J. Cava, C. Felser, B. Yan, S. A. Medvedev, *Nat. Commun.* **2016**, *7*, 11038.
- [40] T. Y. Kim, M. Amani, G. H. Ahn, Y. Song, A. Javey, S. Chung, T. Lee, *ACS Nano* **2016**, *10*, 2819.
- [41] R. Kappera, D. Voiry, S. E. Yalcin, B. Branch, G. Gupta, A. D. Mohite, M. Chhowalla, *Nat. Mater.* **2014**, *13*, 1128.
- [42] R. Ma, H. Zhang, Y. Yoo, Z. P. Degregorio, L. Jin, P. Golani, J. G. Azadani, T. Low, J. E. Johns, L. A. Bendersky, A. V. Davydov, S. J. Koester, *ACS Nano* **2019**, *13*, 8035.
- [43] S. Yang, X. Xu, W. Xu, B. Han, Z. Ding, P. Gu, P. Gao, Y. Ye, *ACS Appl. Nano Mater.* **2020**, *3*, 10411.
- [44] S. Y. Chen, T. Goldstein, D. Venkataraman, A. Ramasubramaniam, J. Yan, *Nano Lett.* **2016**, *16*, 5852.
- [45] R. Beams, L. G. Cançado, S. Krylyuk, I. Kalish, B. Kalanyan, A. K. Singh, K. Choudhary, A. Bruma, P. M. Vora, F. Tavazza, A. V. Davydov, S. J. Stranick, *ACS Nano* **2016**, *10*, 9626.
- [46] E. Artacho, E. Anglada, O. Diéguez, J. D. Gale, A. García, J. Junquera, R. M. Martin, P. Ordejón, J. M. Pruneda, D. Sánchez-Portal, *J. Phys.: Condens. Matter* **2008**, *20*, 064208.
- [47] J. P. Perdew, K. Burke, M. Ernzerhof, *Phys. Rev. Lett.* **1996**, *77*, 3865.
- [48] S. Grimme, *J. Comput. Chem.* **2006**, *27*, 1787.
- [49] H. J. Kim, S. H. Kang, I. Hamada, Y. W. Son, *Phys. Rev. B: Condens. Matter Mater. Phys.* **2017**, *95*, 180101.
- [50] N. Troullier, J. L. Martins, *Phys. Rev. B: Condens. Matter Mater. Phys.* **1991**, *43*, 1993.
- [51] L. Kleinman, D. M. Bylander, *Phys. Rev. Lett.* **1982**, *48*, 1425.
- [52] G. Kresse, J. Furthmüller, *Phys. Rev. B: Condens. Matter Mater. Phys.* **1996**, *54*, 11169.
- [53] G. Kresse, J. Hafner, *Phys. Rev. B: Condens. Matter Mater. Phys.* **1993**, *47*, 558.
- [54] I. Hamada, *Phys. Rev. B: Condens. Matter Mater. Phys.* **2014**, *89*, 121103.